PHYSICAL REVIEW D VOLUME 23, NUMBER 1 1 JANUARY 1981

Large-angle proton-proton elastic scattering at 201 and 400 GeV/c

W. Faissler, M. Gettner, J. R. Johnson,* T. Kephart, E. Pothier, D. Potter,† and M. Tautz
Northeastern University, Boston, Massachusetts 02115

S. Conetti, C. Hojvat,‡ D. G. Ryan, K. Shahbazian, D. G. Stairs, and J. Trischuk
McGill University, Montreal, Quebec H3A 2T8, Canada

P. Baranov,§ J. L. Hartmann, J. Orear, S. Rusakov,§ and J. Vrieslander
Cornell University, Ithaca, New York 14853
(Received 29 August 1980)

Proton-proton elastic scattering using 201- and 400-GeV/c extracted beams at Fermilab has been measured in the region $4.9 < -t < 14.4$ GeV^2. Contrary to predictions of diffraction models, there is no sign of a second dip or "break," and the slope A in the fit $\exp(At)$ is smaller than predicted. It drops from 1.5 to 0.8 GeV^{-2} over our t range. The shape of the t distribution can be fitted by the power law $d\sigma/dt \propto t^{-8.4}$ which is close to a quantum-chromodynamics (QCD) prediction of t^{-8}. At fixed t the 201-GeV/c cross sections are about 2.3 times those at 400 GeV/c which is compatible with the QCD and constituent-interchange-model prediction that $d\sigma/dt \propto s^{-10}$ at fixed t/s.

I. INTRODUCTION

Diffraction-scattering models have been used to interpret elastic scattering at high energies and small momentum transfers. The diffraction-scattering approach successfully predicts forward peaks consistent with the optical theorem which are essentially energy independent (except for effects of the slow increases in the total cross section).[1,2] In the case of proton-proton scattering a dip-bump diffraction pattern was predicted before it was observed. Extension of the diffraction-scattering approach to larger momentum transfer predicted a second dip at $-t \sim 5$ GeV^2 and a slope for $d\sigma/dt$ following the first dip which should be about half the slope of the forward diffraction peak.[1,2]

The main purpose of this experiment is to study the shape of the angular distribution in detail at Fermilab energies and also to study the energy dependence, if any. As will be shown in Sec. IV on results, the diffraction-model predictions of half the slope, followed by a second dip, and little energy dependence are all violated. Our results conform more closely to what is expected using quantum chromodynamics (QCD) and constituent models of the proton.[3]

Some of the results in this paper have been reported in preliminary form.[4,5] This paper presents the completed analysis of all the data and a more detailed discussion of the experimental approach (Sec. II) and theoretical implication (Sec. IV). Additional information on the experimental method and data analysis is contained in Ref. 6.

II. EXPERIMENTAL METHOD

A. The spectrometers

In order to reach cross sections as low as 6×10^{-38} cm^2/GeV^2 in the presence of a total cross section of 4×10^{-26} cm^2 it was necessary to use separate spectrometers for the scattered proton and the recoil proton. Each spectrometer was tuned to the same kinematical region. The master trigger consisted of a fast coincidence between the two spectrometers. Three-dimensional tracks after magnetic deflection were reconstructed using track coordinates obtained from a total of 23 multiwire proportional chambers (MWPC's). A schematic (not to scale) of the two spectrometers is shown in Fig. 1(a). The corresponding scale drawing is shown in Fig. 1(b). The forward arm used three separate dipoles (150 kGm) at 400 GeV/c and two dipoles (90 kGm) at 201 GeV/c. The recoil arm used one dipole of 24×4 in. aperture (~ 40 kGm). As indicated in Fig. 2(b), the acceptance in t of the recoil arm could be changed by varying the target position. However, the only way of changing the t region accepted by the forward arm was by moving the entire arm. Two t regions were covered at 201 GeV/c and three at 400 GeV/c. These are listed in Table I.

Because of the angle-momentum relation, the recoil magnet achieved point-to-parallel focusing in the horizontal plane for elastic but not for inelastic scattering. This permitted smaller-sized detectors for a given t range with corresponding improvement in signal-to-background ratio.

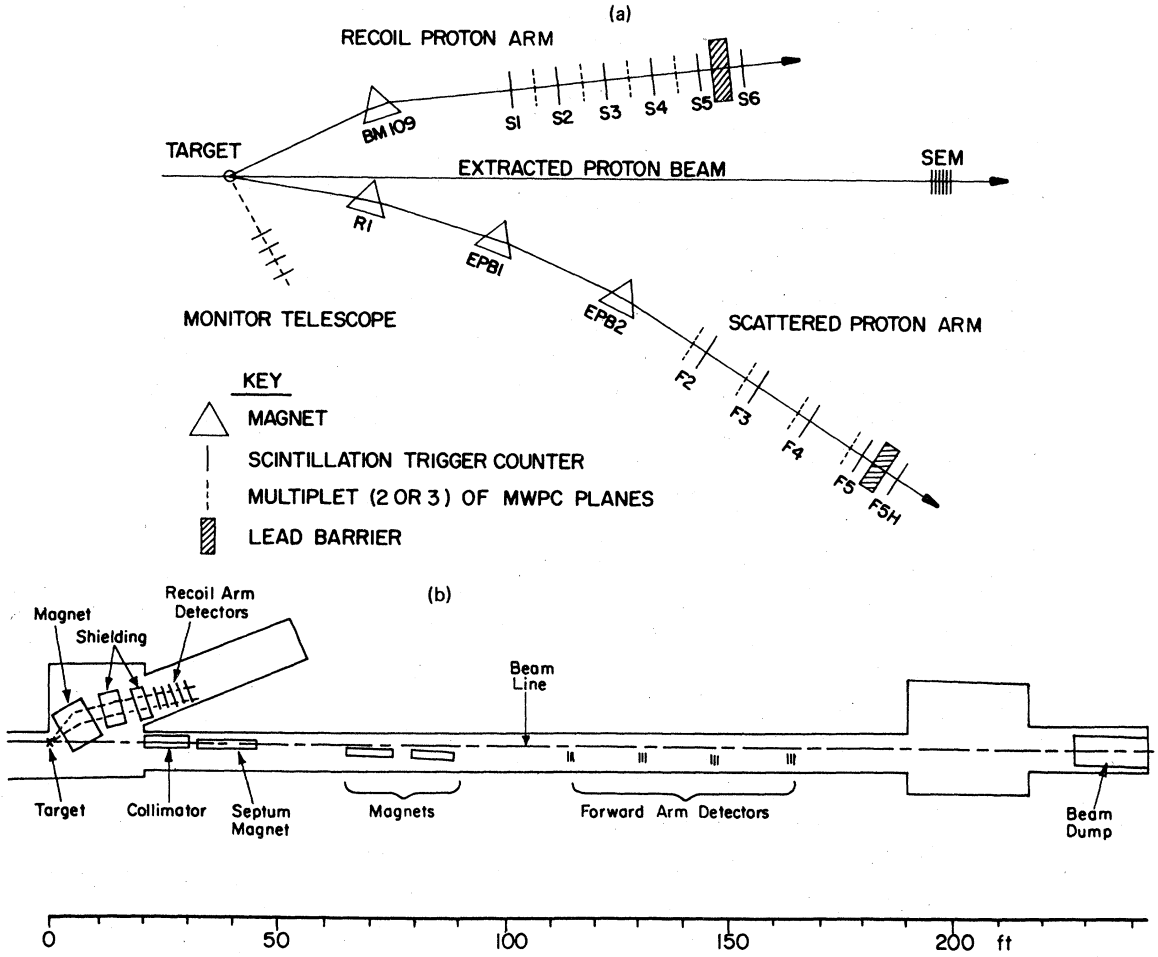

FIG. 1. Plan view of the experiment. (a) Schematic showing relative positions of the apparatus (not to scale). EPB2 was not used in the 201-GeV/c running. (b) Scale drawing showing both forward and recoil spectrometer positions.

B. Beam and shielding

Our 4-in. long liquid-hydrogen target was located in the Fermilab Proton West extracted proton beam line. This beam line was optimized for low emittance, low halo, and high intensity. Our typical spot size was of diameter ~ 4 mm full width at half maximum. At 400 GeV/c the emittance was 0.46 mm mrad horizontal and 0.28 mm mrad vertical. Our apparatus could handle beam intensities up to ~ 7×10^{11} protons/pulse, but only after taking various precautions with shielding. As shown in Fig. 2(a), the forward spectrometer was shielded by a 3-m-long iron collimator with aperture tightly fitted to the t range in use. It also contained a tapered beam pipe, the diameter of which was adjusted to minimize rates in the trigger counters. A small-angle particle from the target would either be intercepted by the beam-pipe inserts or would travel in vacuum past the detectors. Aluminum and brass collimators were inserted in all bending magnets. A series of lead brick tunnels were built to surround the forward-arm detectors with at least 4 in. of lead on four sides. Although none of the forward-arm detectors could directly "see" the target, each was subject to particles caused by illumination of the collimator surfaces and magnet pole faces. The use of successive bending magnets swept out much of this background. Figure 2(b) shows some of the concrete shielding installed in order to reduce singles rates due to slow neutrons. None of the singles rates exceeded 5×10^6 counts/sec.

C. Detectors

The master trigger consisted of a coincidence between the forward-arm trigger and the recoil-arm trigger. The forward-arm trigger was a fivefold coincidence among five scintillation counters and the recoil-arm trigger was a similar sixfold coincidence. The last counter of each arm

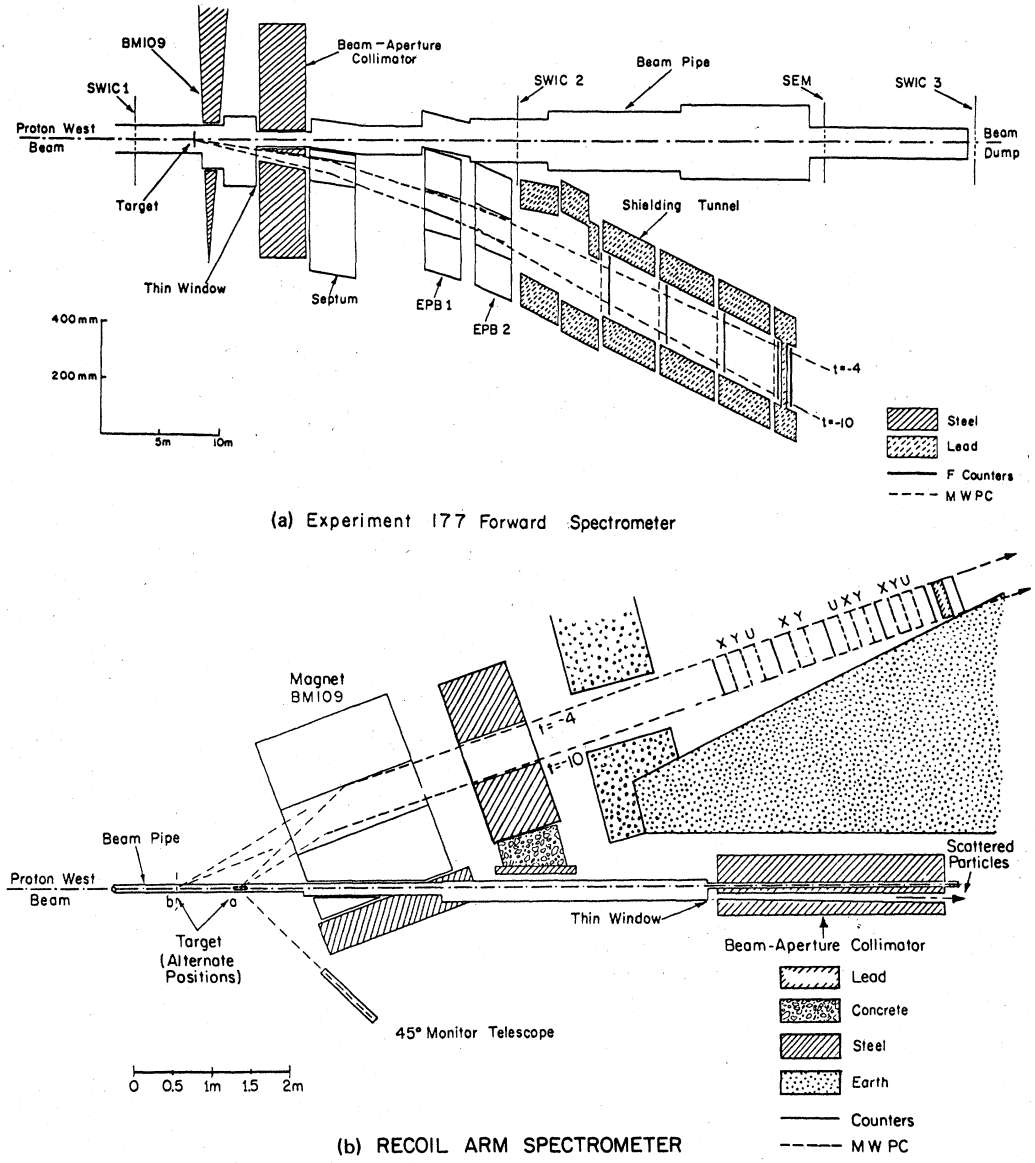

FIG. 2. Shielding and beam-pipe details of the spectrometers. (a) Forward spectrometer. Note the magnified vertical scale. (b) Recoil spectrometer. Target position a covers $4 < -t < 10$ GeV^2 and position b covers $8 < -t < 15$ GeV^2. Note the point-to-parallel optics due to elastic kinematics.

TABLE I. The five geometries, their t range, total numbers of beam particles, and background under the elastic peak.

Geometry	t range (GeV^2)	N_b	Inelastic background (percent)
201 low t	4.9– 8.3	6.4×10^{15}	0%
201 high t	7.7–12.1	2.3×10^{16}	2 ± 1%
400 low t	5.4– 9.2	3.5×10^{15}	12 ± 2%
400 mid t	8.4–12.8	2.1×10^{16}	6 ± 2%
400 high t	10.0–14.4	4.7×10^{16}	4 ± 1%

was positioned behind a lead barrier (10 in. thick in the forward arm, 4 in. in the recoil arm) in order to obtain rejection of electrons originating mainly from γ's from π^0 decay. Comparison runs were performed to verify that these barriers were not causing the loss of elastic events.

The MWPC's were $\frac{1}{4}$ in. thick with 16 wires per inch. Both arms had four x chambers and four y chambers (reading horizontal and vertical coordinates, respectively). The forward and recoil arms had four and three u chambers, respectively (wires at 45° to x and y). Each wire was supplied

with an amplifier, threshold discriminator, one-shot generated adjustable delay, and a gated latch. In order to reduce local deadtime due to long cable delays to and from the control room, pretriggers were formed for each arm separately using nearby coincidence circuits which generated gate pulses for the latches. These pulses arrived at their corresponding MWPC's about 300 nsec after the actual hit. The one-shot delays in each chamber were adjusted to supply the signal pulse to the latch at the same time as arrival of the pretrigger gate pulse. The resolving time was given by the width of the latch gate pulse which was set at 100 nsec. A conceptual schematic of the fast electronics is shown in Fig. 3. The latches were held for a time long enough to form the master trigger and send back a read-out pulse from the control room. The typical data-taking rate was ~ 30 triggers per beam pulse. During this dead time the beam monitor telescope which viewed the hydrogen target was gated off.

A more detailed description of the MWPC read-out system and the on-line computer system (PDP-11/45) is given in Ref. 6. In addition to data recording on magnetic tape, the on-line system provided continuous equipment monitoring and diagnostics. Beam normalization was obtained using the ratio of gated to ungated monitor-telescope counts compared to an ungated secondary-emission monitor (SEM) located in the beamline. This device was calibrated by placing copper foils over its aperture during calibration runs where the integrated SEM counts were compared with the activation level of the foils. The absolute copper activation cross section[7] at 200 and 400 GeV/c provided the factor needed to convert SEM counts to number of beam protons.

III. ANALYSIS

A. Selection of elastic events

There are two main tasks for the analysis of the records on the data tapes: (1) selection of elastic events, and (2) computation of absolute cross sections. Most data events were produced by assorted combinations of random coincidences where one or more extraneous particles would traverse several trigger counters. Most of the remaining events consisted of "spray" from collimators or magnet polefaces. To save computing time and tape handling during the early phase of the off-line analysis summary tapes were produced containing only those events which had at least one track per arm passing certain aperture cuts. This alone was an extremely powerful selection criterion; viz., about 45% of the remaining 201-GeV/c events were elastic. For 400 GeV/c the corresponding figure was ~ 10%. This shows the power of the trigger system alone in selecting elastic events out of inelastic processes.

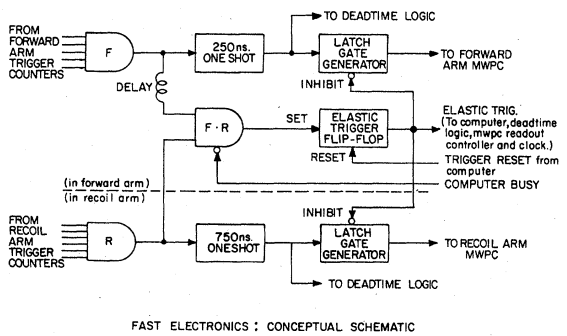

FIG. 3. Conceptual schematic of the fast electronics showing how pretriggers and the master trigger are formed.

The selection criteria used to define a track in the forward arm were that any three out of four x coordinates lie on straight lines. Only those x and y line pairs were used which agree with any of the u tracks. With each plane running at about 94% efficiency, the overall track-finding efficiency for both arms jointly was 88% using this and a similar algorithm for the recoil arm.

The momentum and production angle of each forward track was determined by assuming it originated from the target center ($x = z = 0$). Momentum distributions of the forward track for two different geometries are shown in Fig. 4(a). (The subscripts f and r stand for forward and recoil arm, respectively.) In each case there is a peak at the predicted momentum corresponding to elastic scattering. In some cases the background under the peak is as high as 60%. However, by using information from tracks in the recoil arm, this background is reduced to a few percent [see Fig. 4(b)]. The background levels are listed in Table I. The full information obtained from this target-center ana-

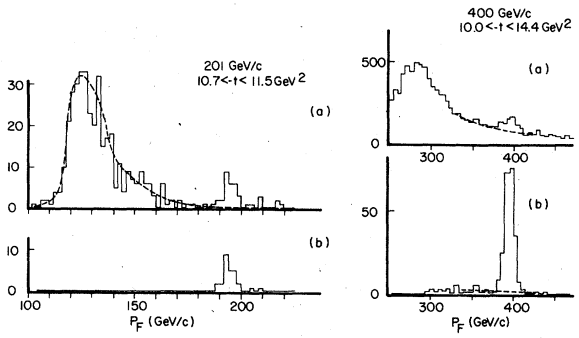

FIG. 4. (a) Momentum distribution in the forward arm before making elastic cuts. All events are used where there is at least one track in each arm appearing to originate from the target. (b) Same as (a) except that coplanarity, Δy, Δt, and missing-mass cuts have been made.

lysis gives θ, ϕ, p, and y for each track where θ is the polar angle between the nominal beam direction and the direction of the particle after scattering, ϕ is the azimuth angle with respect to the horizontal plane, p is the particle momentum, and y is the height of the track when x and $z = 0$ (z is along beam direction measured from the target center).

Using p and θ one can calculate the corresponding four-momentum transfer t and the missing mass. In Fig. 4(b) the same events shown in Fig. 4(a) have been subjected to the following cuts: MMSQ (missing mass squared of the forward particle using P_r and θ_r), $\Delta t \equiv t_f - t_r$, $\Delta\phi \equiv \phi_f - \phi_r$ (coplanarity), and $\Delta y \equiv y_f - y_r$. This last test is the difference in height of the interaction point as indicated by the forward and recoil track. In most cases the above cuts were set at about 3 standard deviations from the mean. Sample histograms of Δt, $\Delta\phi$, and Δy are shown in Fig. 5. Elastic events are selected making all five cuts: p_f, MMSQ, Δt, $\Delta\phi$, and Δy.

Although the above procedure does a clean job of extracting the rare elastic events out of millions of triggers, it does not give as accurate an estimate of t as can be obtained from the data. A more accurate determination can be made by relaxing the point-target constraint on the forward particle and replacing it with the angle-momentum constraint of elastic scattering. In this procedure one assumes the forward-particle has the elastic-scattering momentum corresponding to the θ obtained from the original point-target approximation. Then the forward particle is again tracked back to the target region giving a new value for θ. Using elastic kinematics this gives a new value for momentum and the above procedure is repeated a total of five times (this ensures convergence). The t resolution obtained from this iteration procedure is about three times better than that using the point-target approximation. Our final estimated t resolution as a function of t is shown in Fig. 6. It is always less than the bin width used in Table II.

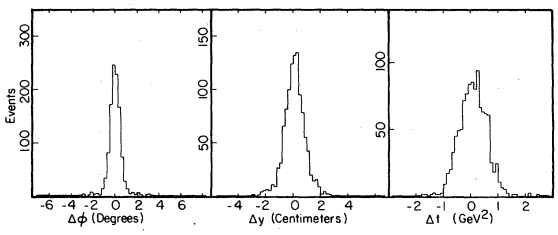

FIG. 5. Coplanarity, Δy, and Δt, histograms for events obtained using the 201-GeV/c hi-t geometry. In each case cuts on all variables including P_f have been made except for $\Delta\theta$ and the variable which is plotted.

Using the more refined values of p_f and θ_f obtained by the above iteration procedure, a sixth and final cut was made on the elastic candidates. This was $\Delta\theta_r \equiv \theta_r$ (measured) $- \theta_r$ (predicted), where θ_r (measured) is the θ_r obtained by tracking using p_r obtained from the refined p_f and where θ_r (predicted) is the predicted value of θ_r obtained from the refined θ_f using elastic kinematics. The surviving number of events per bin is listed in Table II.

B. Cross sections

The number of elastic events observed in a bin of width Δt is

$$\Delta N(t) = N_b N_t \frac{d\sigma(t)}{dt} \Delta t \frac{\Delta\phi(t)}{2\pi} E,$$

where

N_b = beam passing through target during the time the logic is gated on,
$N_t = 4.31\times10^{23}$ protons/cm^2 (target thickness).
$d\sigma(t)/dt$ = differential cross section for pp elastic scattering over the t bin.
Δt = full width of t bin.
$\Delta\phi(t)/2\pi$ = geometrical acceptance (fractional azimuthal bite), and
E = total apparatus efficiency
$= \varepsilon(1-l_n)(1-l_r)(1-l_p)(1-l_c)$, where
ε = track-finding efficiency (using measured MWPC efficiencies) = $88\pm4\%$,
l_n = fraction of elastic events lost because either particle interacted and got "lost" = $16\pm2\%$,
l_r = fraction of elastic events lost due to MWPC-readout failures = 2%,
l_p = fraction of elastic events lost due to multiple tracks (picking wrong track when arm has more than one) = $3\pm1\%$, and
l_c = fraction of elastic events lost due to elastic cuts = $4.5\pm1\%$.

No correction was made for possible counting loss.

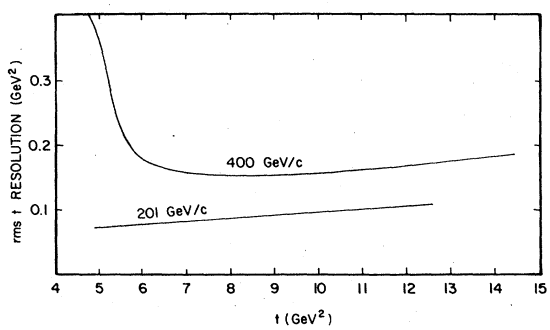

FIG. 6. t resolution as a function of t for 201 and 400 GeV/c.

TABLE II. Differential cross sections for the five geometrics specified in Table I. N is the number of events per bin surviving the elastic cuts (before making the small correction for inelastic background). $\Delta\phi/2\pi$ is the geometrical acceptance factor plotted in Fig. 7. Except for the two lowest t points, the quoted errors are statistical only. In addition there is an overall normalization error of ±15%.

Bin center t (GeV^2)	Bin width Δt (GeV^2)	No. of events N	Acceptance $\frac{\Delta\phi}{2\pi}$	$\frac{d\sigma}{dt}$ (cm^2/GeV^2)
201 low t				
5.0	0.2	1786	8.01×10^{-3}	$7.08 \pm 0.24 \times 10^{-34}$
5.2	0.2	1587	8.20×10^{-3}	$6.15 \pm 0.22 \times 10^{-34}$
5.4	0.2	1074	8.26×10^{-3}	$4.12 \pm 0.15 \times 10^{-34}$
5.6	0.2	837	8.32×10^{-3}	$3.19 \pm 0.11 \times 10^{-34}$
5.8	0.2	629	8.38×10^{-3}	$2.38 \pm 0.10 \times 10^{-34}$
6.0	0.2	432	8.44×10^{-3}	$1.63 \pm 0.07 \times 10^{-34}$
6.2	0.2	392	8.50×10^{-3}	$1.46 \pm 0.07 \times 10^{-34}$
6.4	0.2	297	8.56×10^{-3}	$1.10 \pm 0.06 \times 10^{-34}$
6.6	0.2	219	8.62×10^{-3}	$8.07 \pm 0.55 \times 10^{-35}$
6.8	0.2	181	8.68×10^{-3}	$6.62 \pm 0.50 \times 10^{-35}$
7.0	0.2	150	8.74×10^{-3}	$5.45 \pm 0.45 \times 10^{-35}$
7.2	0.2	122	8.80×10^{-3}	$4.41 \pm 0.40 \times 10^{-35}$
7.4	0.2	109	8.86×10^{-3}	$3.91 \pm 0.37 \times 10^{-35}$
7.6	0.2	66	8.92×10^{-3}	$2.35 \pm 0.29 \times 10^{-35}$
7.8	0.2	56	8.98×10^{-3}	$1.99 \pm 0.27 \times 10^{-35}$
8.0	0.2	46	9.04×10^{-3}	$1.61 \pm 0.24 \times 10^{-35}$
8.2	0.2	46	8.52×10^{-3}	$1.71 \pm 0.25 \times 10^{-35}$
201 high t				
7.8	0.2	222	8.92×10^{-3}	$2.26 \pm 0.16 \times 10^{-35}$
8.0	0.2	149	8.95×10^{-3}	$1.50 \pm 0.12 \times 10^{-35}$
8.2	0.2	108	8.98×10^{-3}	$1.09 \pm 0.11 \times 10^{-35}$
8.4	0.2	128	9.01×10^{-3}	$1.29 \pm 0.12 \times 10^{-35}$
8.6	0.2	83	9.04×10^{-3}	$8.32 \pm 0.09 \times 10^{-36}$
8.8	0.2	56	9.07×10^{-3}	$5.59 \pm 0.76 \times 10^{-36}$
9.0	0.2	56	9.10×10^{-3}	$5.58 \pm 0.75 \times 10^{-36}$
9.2	0.2	51	9.13×10^{-3}	$5.07 \pm 0.71 \times 10^{-36}$
9.4	0.2	21	9.16×10^{-3}	$2.07 \pm 0.46 \times 10^{-36}$
9.6	0.2	48	9.19×10^{-3}	$4.73 \pm 0.68 \times 10^{-36}$
9.8	0.2	26	9.22×10^{-3}	$2.56 \pm 0.50 \times 10^{-36}$
10.0	0.2	23	9.25×10^{-3}	$2.25 \pm 0.47 \times 10^{-36}$
10.3	0.4	35	9.29×10^{-3}	$1.70 \pm 0.30 \times 10^{-36}$
10.7	0.4	28	9.35×10^{-3}	$1.35 \pm 0.25 \times 10^{-36}$
11.1	0.4	17	9.41×10^{-3}	$8.18 \pm 1.99 \times 10^{-37}$
11.5	0.4	17	9.47×10^{-3}	$8.14 \pm 1.97 \times 10^{-37}$
11.9	0.4	8	9.53×10^{-3}	$3.80 \pm 1.35 \times 10^{-37}$
400 low t				
5.5	0.2	314	9.17×10^{-3}	$1.76 \pm 0.12 \times 10^{-34}$
5.7	0.2	221	9.65×10^{-3}	$1.18 \pm 0.09 \times 10^{-34}$
5.9	0.2	202	9.78×10^{-3}	$1.06 \pm 0.08 \times 10^{-34}$
6.1	0.2	103	9.82×10^{-3}	$5.39 \pm 0.53 \times 10^{-35}$
6.3	0.2	102	9.61×10^{-3}	$5.45 \pm 0.53 \times 10^{-35}$
6.5	0.2	63	9.46×10^{-3}	$3.42 \pm 0.43 \times 10^{-35}$
6.7	0.2	55	9.43×10^{-3}	$2.99 \pm 0.41 \times 10^{-35}$
6.9	0.2	37	9.46×10^{-3}	$2.01 \pm 0.34 \times 10^{-35}$
7.1	0.2	26	9.49×10^{-3}	$1.40 \pm 0.27 \times 10^{-35}$
7.3	0.2	22	9.52×10^{-3}	$1.19 \pm 0.25 \times 10^{-35}$
7.5	0.2	25	9.56×10^{-3}	$1.34 \pm 0.27 \times 10^{-35}$
7.7	0.2	18	9.60×10^{-3}	$9.63 \pm 2.27 \times 10^{-36}$
7.9	0.2	14	9.64×10^{-3}	$7.45 \pm 1.99 \times 10^{-36}$
8.1	0.2	15	9.68×10^{-3}	$7.96 \pm 2.05 \times 10^{-36}$
8.3	0.2	17	9.72×10^{-3}	$8.98 \pm 2.17 \times 10^{-36}$
8.6	0.4	12	9.80×10^{-3}	$3.14 \pm 0.91 \times 10^{-36}$
9.0	0.4	9	9.88×10^{-3}	$2.33 \pm 0.78 \times 10^{-36}$

TABLE II. (*Continued.*)

Bin center t (GeV^2)	Bin width Δt (GeV^2)	No. of events N	Acceptance $\frac{\Delta\phi}{2\pi}$	$\frac{d\sigma}{dt}$ (cm^2/GeV^2)
400 mid t				
8.6	0.4	86	9.38×10^{-3}	$4.51 \pm 0.48 \times 10^{-36}$
9.0	0.4	61	9.53×10^{-3}	$3.14 \pm 0.40 \times 10^{-36}$
9.4	0.4	28	9.68×10^{-3}	$1.43 \pm 0.27 \times 10^{-36}$
9.8	0.4	25	9.83×10^{-3}	$1.25 \pm 0.25 \times 10^{-36}$
10.2	0.4	17	9.97×10^{-3}	$8.38 \pm 2.04 \times 10^{-37}$
10.6	0.4	8	1.01×10^{-2}	$3.89 \pm 1.38 \times 10^{-37}$
11.0	0.4	14	1.03×10^{-2}	$6.71 \pm 1.79 \times 10^{-37}$
11.4	0.4	6	1.04×10^{-2}	$2.83 \pm 1.16 \times 10^{-37}$
11.8	0.4	3	1.06×10^{-2}	$1.39 \pm 0.81 \times 10^{-37}$
12.2	0.4	3	1.07×10^{-2}	$1.38 \pm 0.79 \times 10^{-37}$
12.6	0.4	4	1.09×10^{-2}	$1.81 \pm 0.91 \times 10^{-37}$
400 high t				
10.2	0.4	46	9.74×10^{-3}	$1.04 \pm 0.15 \times 10^{-36}$
10.6	0.4	43	9.82×10^{-3}	$9.30 \pm 1.42 \times 10^{-37}$
11.0	0.4	18	9.89×10^{-3}	$3.86 \pm 0.91 \times 10^{-37}$
11.4	0.4	23	9.97×10^{-3}	$4.89 \pm 1.02 \times 10^{-37}$
11.8	0.4	11	1.00×10^{-2}	$2.32 \pm 0.70 \times 10^{-37}$
12.2	0.4	12	1.01×10^{-2}	$2.52 \pm 0.73 \times 10^{-37}$
12.6	0.4	4	1.02×10^{-2}	$8.32 \pm 4.16 \times 10^{-38}$
13.0	0.4	7	1.03×10^{-2}	$1.44 \pm 0.55 \times 10^{-37}$
13.4	0.4	3	1.04×10^{-2}	$6.15 \pm 3.55 \times 10^{-38}$
13.8	0.4	6	1.04×10^{-2}	$1.22 \pm 0.50 \times 10^{-37}$
14.2	0.4	5	1.05×10^{-2}	$1.01 \pm 0.45 \times 10^{-37}$

For the following reasons we feel this experiment was free from counting loss: (1) No anticounters were used, (2) all trigger-counter pulses were fanned out into analog-to-digital convertors and to updating discriminators which were continuously monitored, (3) high current bases were used for the photomultiplier tubes, and (4) a plot of the elastic-event rate vs the gated-beam intensity showed no departure from linearity.

Note that $\Delta N(t)$ is the number of elastic events remaining after subtracting the small amount of background under the elastic peak. The differential cross section is thus

$$\frac{d\sigma(t)}{dt} = \frac{\Delta N(t)}{\Delta t N_b N_t (\Delta\phi/2\pi) E} .$$

The values obtained using this formula are listed in Table II along with t, Δt, $\Delta\phi/2\pi$, and ΔN (not corrected for background under the elastic peak). The Monte Carlo determination of $\Delta\phi/2\pi$ for the 400-GeV/c mid-t geometry is shown in Fig. 7, accounting for target size, beam-spot size, beam divergence, and multiple scattering. The same Monte Carlo simulation was also used to compute the smearing effect due to the finite t resolution: Since $d\sigma/dt$ is dropping with t, more events scattered into a given t bin than scattered out. This smearing correction is most serious at the low-t end of the acceptance region. For this reason we have increased the errors of the two lowest t points at 201 and 400 GeV/c by 1%. The remaining errors in Table II are purely statistical. In addition there is an overall normalization error of 15% due to uncertainties in the various effici-

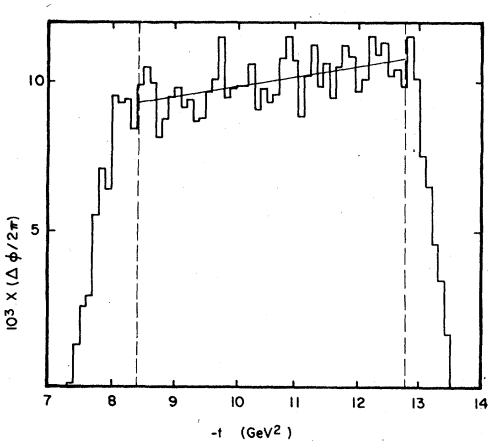

FIG. 7. Geometrical acceptance as generated by our Monte Carlo program for the 400-GeV/c mid-t geometry. Only the region between the dashed lines was used. The sloping line is the least-squares fit used in the analysis.

ency factors plus the 10% uncertainty in the SEM calibration.[7] In taking ratios of 201- to 400-GeV/c cross sections we estimate only a 5% contribution due to normalization uncertainties. The systematic uncertainty in t value for 201 GeV/c is 0.05 GeV^2 and for 400 GeV/c it is 0.08 GeV^2.

IV. RESULTS

The values of $d\sigma/dt$ from the five different geometries of Table II are plotted vs t in Fig. 8. These geometries overlap in three different places. The fact that the cross sections are the same within statistics in the regions of overlap gives independent confirmation of the experimental technique.

Several features of our results are readily apparent from Fig. 8. They are the following.

(a) No evidence of a second dip.

(b) The slope parameter A in $d\sigma/dt \propto \exp(At)$ is 1.5 GeV^{-2} at $-t \approx 5$ GeV^2 and decreases to 0.8 GeV^{-2} at $-t \approx 13$ GeV^2. (Detailed slope parameters are given in Table III.) Our results rule out a slope of ~ 6 GeV^{-2} (half the forward peak slope).

(c) There is still an energy dependence at all t values covered in this experiment. The ratio of $d\sigma/dt$ at 201 GeV/c to that at 400 GeV/c for the same t is about 2.3.

All three of these features are contrary to the predictions of most diffraction models.[1,2]

More information on energy dependence at fixed t is obtained by plotting our data along with previous data at 19.3 (Ref. 8), 21.3 (Ref. 9), 29 (Ref. 10), and 1485 GeV/c (Ref. 11) (equivalent CERN ISR laboratory energy). Comparison of our 400-GeV/c and the 1485-GeV/c ISR results indicates a small energy dependence beyond 400 GeV/c for $5 < t < 8$ GeV^2. The ratio of $d\sigma/dt$ at 400 GeV/c to that of 1485 GeV/c is 1.5 ± 0.3 after taking into account the normalization errors quoted in both experiments. This fading away of the energy dependence is more apparent in Fig. 9 where $d\sigma/dt$ is plotted vs the beam momentum for different fixed values of t. For $-t = 3.6$ GeV^2, $d\sigma/dt$ becomes energy independent at $P_{\text{beam}} \sim 200$ GeV/c and for $-t = 6$ GeV^2, energy independence may set in at $P_{\text{beam}} \sim 1000$ GeV/c. One can at least conclude that the energy dependence is significantly less for $P_{\text{beam}} > 400$ GeV/c than it is for $P_{\text{beam}} < 400$ GeV/c.

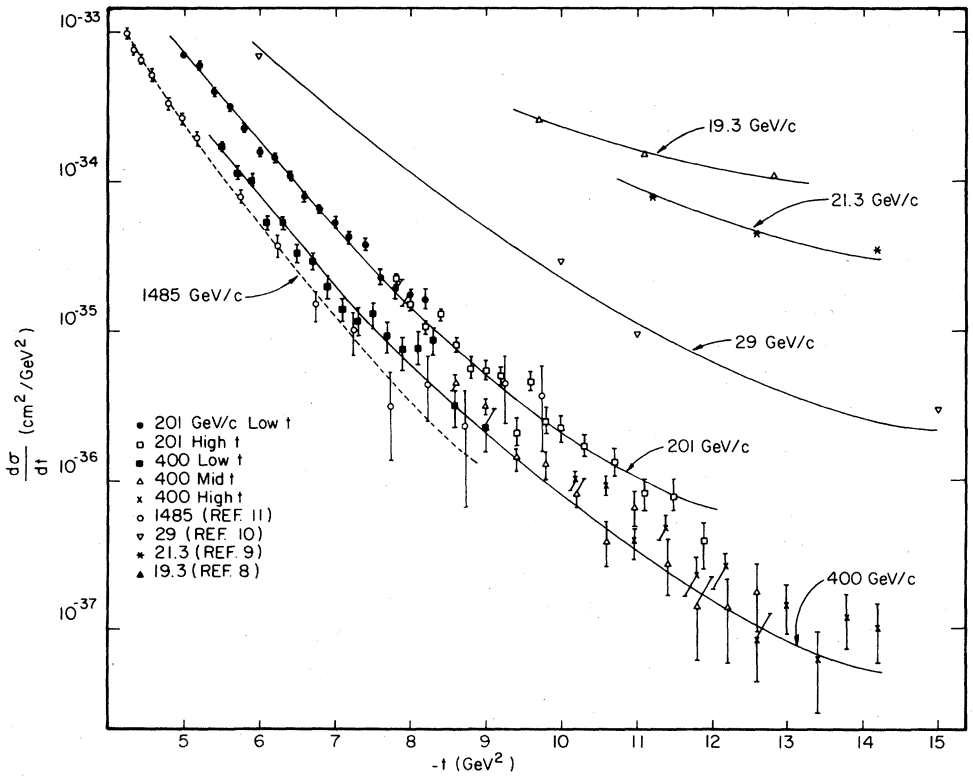

FIG. 8. Our cross sections for all five geometries plotted vs t. Note agreement in regions of overlap. Some data at four other energies are also shown. The curves are drawn to guide the eye.

TABLE III. Slope parameter A obtained from two-parameter least-squares fits to $d\sigma/dt = C\exp(At)$.

Beam momentum (GeV/c)	t range (GeV^2)	A (GeV^{-2})
201	4.9– 6.1	1.46 ± 0.04
201	10.1–12.1	0.85 ± 0.18
400	5.3– 7.0	1.55 ± 0.07
400	10.0–14.4	0.79 ± 0.06

We have shown that $d\sigma/dt$ as a function of t cannot be fit by the function $\exp(At)$ where A is a constant. Another popular function is $d\sigma/dt \propto \exp(-Bp_t)$, where P_t is the transverse momentum of either scattered proton. In Fig. 10 $d\sigma/dt$ is plotted vs P_t. In the regions of overlap we use weighted averages of our cross sections. We see that the data at quite different beam energies lie close to straight lines all having the same slope $B = 6.5$ GeV/c^{-1}. An even better fit can be made to our 400 GeV/c data by using the function $d\sigma/dt \propto t^{-n}$. Here a least-squares fit gives $n = 8.45 \pm 0.1$ with $\chi^2 = 33$ for 28 degrees of freedom. A QCD multiple-gluon-exchange calculation[3] predicts a lowest-order term $d\sigma/dt \propto t^{-8}$ when $-t/s \ll 1$ and $-t \gg 1$ GeV^2. The t^{-n} form when fit to the 201-GeV/c data gives $n = 8.34 \pm 0.07$ with $\chi^2 = 75$ for 28 degrees of freedom. Contrary to the predictions of Ref. 3, we observe an s dependence as well as the t dependence. The combined s and t dependence we observe is consistent with QCD.[12]

The constituent-interchange model predicts $d\sigma/dt \propto 1/s^{n-2}$ at fixed t/s (same as fixed $\theta_{\text{c.m.}}$), where n is the number of incoming plus outgoing quarks.[13] Thus for pp elastic scattering at large t the prediction is that $d\sigma/dt \propto s^{-10} f(t/s)$. In Fig. 11, where $d\sigma/dt$ is plotted vs t/s using logarithmic scales, our 201- and 400-GeV/c data overlap in the region $0.013 < -t/s < 0.018$ ($13.3° < \theta_{\text{c.m.}} < 15.8°$). In the region of overlap the 400-GeV/c data are a factor of 730 below the 201-GeV/c data which corresponds to $s^{-9.6}$ energy dependence.

These results suggest that all 60 experimental points of both 201 and 400 GeV/c can be reasonably

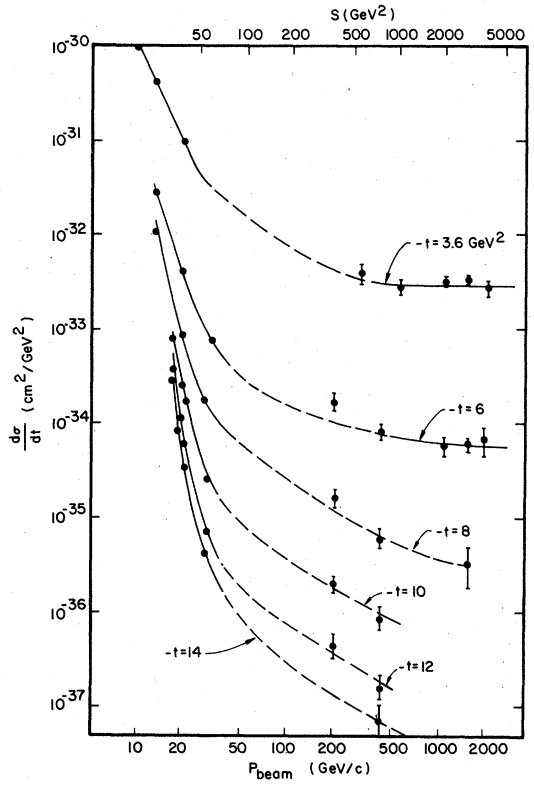

FIG. 9. $d\sigma/dt$ vs P_{beam} is plotted using logarithmic scales for $-t = 3.6$, 6, 8, 10, and 12 GeV^2. Some of the points shown are interpolations from nearby experimental points. Curves are drawn to guide the eye. If the Regge form $d\sigma/dt \propto s^{2\alpha(t)-2}$ were valid, these curves would be straight lines.

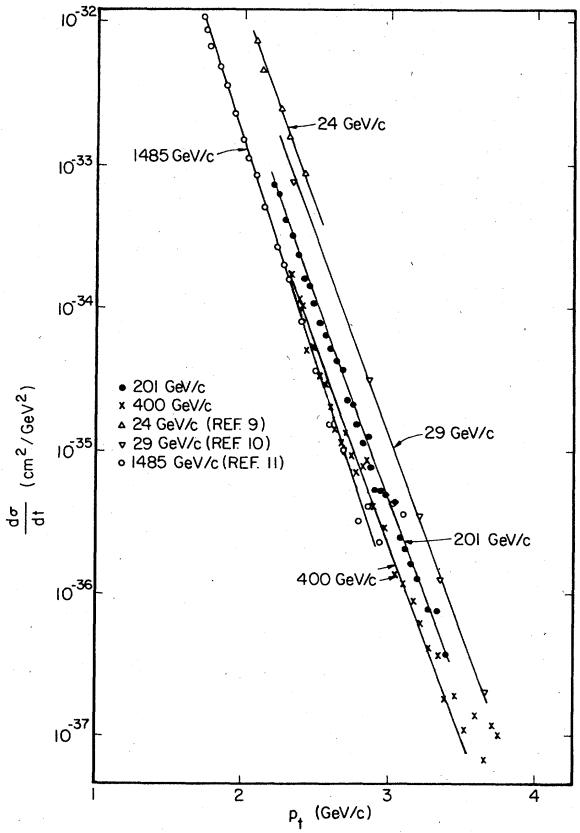

FIG. 10. $d\sigma/dt$ plotted vs transverse momentum. The straight lines at beam momenta of 24, 29, 201, and 400 GeV/c all have slope 6.5 GeV/c^{-1}. The straight line for the ISR data at 1485 GeV/c has slope 7.1 GeV/c^{-1}.

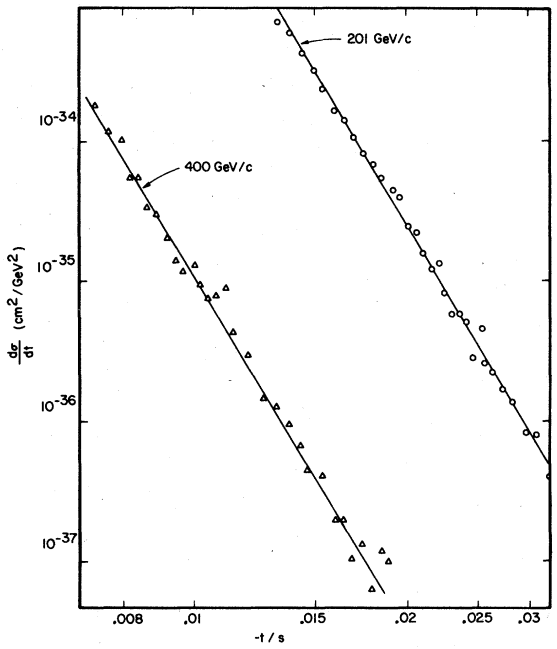

FIG. 11. $d\sigma/dt$ is plotted vs t/s using logarithmic scales. The slope of each of the straight lines is such that $d\sigma/dt \propto (1/t)^{8,37}$. The line separation is such that $d\sigma/dt \propto (1/s)^{9,6}$ for fixed (t/s) (same as fixed $\theta_{\text{c.m.}}$).

fit by the form

$$d\sigma/dt = C(1\ \text{GeV}^2/s)^a f(t/s),$$

where $f(t/s) = (-s/t)^b$. The least-squares solution is $a = 9.6 \pm 0.1$, $b = 8.37 \pm 0.06$, and $C = (7.04 \pm 0.11) \times 10^{-25}$ cm^2/GeV^2 which gives a χ^2 value of 110. Since systematic errors were ignored for 56 of the points, this χ^2 result of 1.8 per degree of freedom is about as good as can be achieved using any other smooth function. This function generates the two straight lines shown in Fig. 11.

There are a number of modified diffraction-type models which fit aspects of our data. Some are diffraction models with a smaller core region.[14,15] Another diffraction approach is to invoke multiple scattering of N constituents, yielding the result $N = 3$.[16] The transition from the diffraction region to the constituent region is discussed in Refs. 17 and 18.

ACKNOWLEDGMENTS

We wish to thank B. Cox, T. Murphy, J. Peoples, R. Rubinstein, R. Schaeren, and the Proton Laboratory staff for their help and cooperation. This work was supported in part by the U. S. National Science Foundation, the National Research Council of Canada through the Institute of Particle Physics, and the Ministry of Education of Quebec.

---

*Present address: University of Wisconsin, Madison, Wisconsin 53706.
†Present address: Rutgers University, New Brunswick, New Jersey 08903.
‡Present address: Fermilab, Batavia, Illinois 60510.
§Permanent address: Lebedev Physical Institute, Moscow, U. S. S. R.

[1] T. T. Chou and C. N. Yang, Phys. Rev. D 17, 1889 (1978).
[2] U. P. Sukhatme, Phys. Rev. Lett. 38, 124 (1977).
[3] A. Donnachie and P. V. Landshoff, Z. Phys. C 2, 55 (1979).
[4] J. Hartmann *et al.*, Phys. Rev. Lett. 39, 975 (1977).
[5] S. Conetti *et al.*, Phys. Rev. Lett. 41, 924 (1978).
[6] J. Vrieslander, Ph.D. thesis, Cornell University (unpublished).
[7] A. Chapman *et al.*, Report No. CERN SPS/ABT/INT 79-1 (unpublished); also private communication from S. Baker of Fermilab.
[8] J. V. Allaby *et al.*, Phys. Lett. 25B, 156 (1967).
[9] J. V. Allaby *et al.*, Nucl. Phys. B52, 316 (1973).
[10] G. Cocconi *et al.*, Phys. Rev. 138, 164B (1965).
[11] H. DeKerret *et al.*, Phys. Lett. 68B, 374 (1977).
[12] P. Lepage and S. Brodsky, Phys. Rev. D 22, 2157 (1980).
[13] D. Sivers, S. J. Brodsky, and R. Blankenbecler, Phys. Rep. 23C, 1 (1976). Also see Ref. 3.
[14] J. Orear, Phys. Rev. D 18, 2484 (1978).
[15] G. W. Heines and M. M. Islam, University of Connecticut report, 1979 (unpublished).
[16] S. Wakaizumi and M. Tanimoto, Phys. Lett. 70B, 55 (1977).
[17] D. D. Coon, J. F. Gunion, J. T. T. Van, and R. Blankenbecler, Phys. Rev. D 18, 1451 (1978); Y. Afek, C. Leroy, B. Margolis, and P. Valin, Phys. Rev. Lett. 45, 85 (1980).
[18] S. V. Goloskokov, S. P. Kuleshov, and O. V. Seljugin, Dubna Report No. E2-12605, 1979 (unpublished).